Understanding the Role of Lithium Borate as the Surface Coating on High Voltage Single Crystal LiNi$_{0.5}$Mn$_{1.5}$O$_4$

Na Ri Park, Yixuan Li, Weiliang Yao, Minghao Zhang, Bing Han, Carlos Mejia,
Baharak Sayahpour, Ryosuke Shimizu, Bhargav Bhamwala, Bryant Dang,
Shinichi Kumakura, Weikang Li,* and Ying Shirley Meng*

The high-voltage spinel lithium nickel manganese oxide (LNMO) with an operating voltage of 4.8 V is a promising cathode material for next-generation lithium-ion batteries (LIBs). However, LNMO/graphite (LNMO/Gr) full cells suffer capacity fading, which limits their practical applications. In this study, lithium metaborate (LBO) is applied on the LNMO surface to improve the full cell performance via a dry mixing method. The LBO-coated LNMO delivers much better cycling stability than the uncoated LNMO in full cells with a practical 3 mAh cm^{-2} areal capacity. Different characterizations are performed to understand the coating effect to track the boron and its impact on the cathode, electrolyte, and anode. The LBO-coated LNMO owns a 5 nm cathode electrolyte interphase (CEI) with mitigated phase change after long-term cycling. The uncoated LNMO has negligible CEI with obvious phase change. However, no boron can be detected on the surface of the coated sample. Electrolyte and anode analyses indicate that the coating acts as an additive reservoir, gradually dissolves into the electrolyte, and generates BF$_4^-$ species. As a result, Nickel/Manganese (Ni/Mn) dissolution from LNMO and the extensive generation of solid electrolyte interphase (SEI) on the anode side is mitigated, thus improving the full-cell cycling stability to a great extent.

N. R. Park, Y. Li, M. Zhang, B. Han, C. Mejia, B. Sayahpour, R. Shimizu,
B. Bhamwala, B. Dang, W. Li, Y. S. Meng
Department of NanoEngineering
University of California San Diego
La Jolla, CA 92093, USA
E-mail: wel001@ucsd.edu; shirleymeng@uchicago.edu
W. Yao
Materials Science and Engineering
University of California San Diego
La Jolla, CA 92093, USA
S. Kumakura
Umicore
Entrance 1A RBM-PCC, Watertorenstreet 37A, Olen 2250, Belgium
Y. S. Meng
Pritzker School of Molecular Engineering
The University of Chicago
Chicago, IL 60637, USA

1. Introduction

The demand for electric vehicles (EVs) has increased significantly due to extensive regulations on CO$_2$ emissions and the rising price of gasoline. However, charging EVs can be inconvenient for customers due to the short mileage per charge and long charging time. To address this issue, many researchers are working on increasing the energy density and fast-charging capability of LIBs. For energy density improvement, increasing the operating voltage of cathode active material is one of the most effective ways, but challenging. First, regular battery electrolyte suffers severe decomposition during high-voltage operation. Second, cathode active materials such as high Ni LiNi$_x$Co$_y$Mn$_z$O$_2$(x + y + z = 1, NCM) are unstable when charged to more than 4.5 V, resulting in fast capacity decay and safety issues. Third, the choice of cathode transition metal composition is important. Cobalt (Co) is commonly used to improve the stability of cathodes, but its price has risen significantly in recent years. As a result, high voltage Co-free spinel material LiNi$_{0.5}$Mn$_{1.5}$O$_4$ (LNMO) has attracted attention,[1] considering its 3D spinel structure for fast charge/discharge, a high working potential of 4.8 V, and a theoretical capacity of 147 mAh g^{-1}.[2] All these advantages enable a significant chance for LNMO to be the cathode active material for next-generation high-voltage LIBs.

However, the practical application of LNMO in full cells is yet to be achieved because of the intrinsic high-voltage operation, which results in fast capacity decay during cycling. Several hypotheses have been proposed to explain the fast degradation: 1) When operating at high voltage, the structure change of the cathode itself is intensified. Mn$_3$O$_4$-like spinel and rock-salt structures are known to form on and below the surface of LNMO particles due to the migration of transition metals to tetrahedral (8a sites) and octahedral sites (16c sites). This irreversible structure change initiated transition metal migration/dissolution, increased charge transfer impedance, and severely degraded battery performance.[3] 2) Choi et al. reported that aging of the LNMO electrode was accelerated at high temperature (i.e., 60 °C)

ADVANCED
SCIENCE NEWS

www.advancedsciencenews.com

ADVANCED
FUNCTIONAL
MATERIALS

www.afm-journal.de

or high voltage due to continuous SEI growth following transition metal redeposition in LNMO/Gr full cell, increasing the surface impedance of the electrode.[4] 3) The capacity fade of the LNMO/Gr full cell resulted from lithium inventory loss. Since active lithium is used to continuously form an interphase in the LNMO/Gr full cell system, the amount is continuously depleted, which eventually affects the long-term cycle.[5] 4) Moreover, the standard electrolyte consisting of organic carbonate solvent and $LiPF_6$ salt is unstable at operating potentials above 4.5 V. The electrolyte decomposition severely triggered the degradation of LNMO/Gr full cell.[6]

Several methods have been verified to improve the cycling performance of LNMO/Gr full cells. First, many strategies have been explored in designing high-voltage electrolytes, including different electrolyte additives. These additives could facilitate stable CEI and SEI, which helped stabilize active materials and prevent dramatic capacity degradation. Cho et al. successfully demonstrated succinic anhydride (SA) and 1,3-propane sultone (PS) additives for improving the electrochemical performance of LNMO/Gr full cells.[7] They proposed that SA and PS could control the swelling behavior of LNMO/Gr cells because of the increased stability against oxidation on the cathode side and robust SEI on graphite. High salt concentration electrolytes (HCE)[8] and ionic liquids[9] have also been explored for high-voltage systems, but both suffer from high viscosity and poor wettability with thick electrodes. The replacement of carbonate-based solvents with fluorinated-based,[10] sulfone-based,[11] or nitrile-based[12] solvents has also been demonstrated, as these solvents typically have very high oxidation stability. However, the practical implementation is challenging due to their expensive price, high viscosity, and low ionic conductivity, which make them difficult to use in practical cells. Second, different LNMO cathode modification methods, including doping and particle size optimization. It was proposed that the dopants could stabilize the LNMO structure, therefore decreasing transition metal dissolution and surface phase change. Okudur et al. doped the LNMO surface with Ti and annealed it in an oxygen atmosphere, resulting in an increase in the Ni–Mn ordering degree of doped LNMO with increasing annealing temperature.[13] Interface stability can be improved with developed intrinsic properties by changing the chemical composition design material of the cathode. Chen et al. synthesized $LiNi_xMn_{2-x}O_4$ ($0.3 \leq x \leq 0.5$) single-crystal samples using molten salt and changed the chemical composition. As a result, the ordering/disordering transition of spinel is affected by the chemical composition. The change in Mn^{3+} content can be induced by optimizing the Ni/Mn ratio through various chemical compositions.[14] Liang et al. used a Ni-Mn compound with a low Mn^{3+} and impurity content as a precursor for the synthesis of LNMO due to the compound's highly crystalline spinel structure.[15] Last, the surface coating has been applied to improve the electrochemical performance of LNMO/Gr full cells. Different coating chemistries have been verified, such as oxides (Al_2O,[16] ZnO,[17] and Bi_2O_3[18]), phosphate,[19,20] and borate[21,22] on the cathode. With all these surface coatings, different improvement mechanisms have been proposed. Gong et al.[21] reported that electrolyte corrosion could be prevented by coating Li_3BO_3 on LNMO using the wet-chemistry method. They claim that the structural stability increases because of the low Mn^{3+} and O vacancy after coating. Roh et al.[22] reported that

the $Li_2O-2B_2O_3$ coating is effective for high-temperature cycling. They mentioned that the coating layer could control the organic CEI layer growth even at high temperatures. Sheen et al.[23] reported that coating the surface of spinel lithium manganese oxide with LBO glass through the solid-state method resulted in good cycle performance. They stated that the improvement was due to reducing the contact with the electrolyte through the physical coating. A literature summary for surface modification on LNMO with different coating materials or methods is shown in Table S1 (Supporting Information), with the proposed mechanism and results. However, several questions must be tackled on the surface-coated LNMO: 1) How to evaluate the surface coating uniformity? 2) is there any change in the surface coating after long-term cycling, and would the change influence the components such as cathode, electrolyte, and anode? 3) how would the surface coating correlate to improved performance?

In this study, we modified the LNMO surface by dry mixing the material with an organic nano-sized boron precursor. The surface coating quality was systematically checked using backscattered scanning electron microscopy (BSE-SEM) and electron energy loss spectra (EELS) from scanning transmission electron microscopy (STEM). It was found that $LiBO_2$ was uniformly distributed on the single-crystal LNMO particle surface, which remarkably improved the cycle stability of LNMO/Gr full cells with 3 mAh cm^{-2} areal capacity. The mechanism was thoroughly investigated using advanced characterizations including SEM, XRD, X-ray photoelectron spectroscopy (XPS), ^{19}F-Nuclear magnetic resonance spectroscopy (NMR), Inductively coupled plasma mass spectrometry (ICP-MS), STEM-EELS. We found that the coating acts as an LBO reservoir to mitigate capacity degradation via HF scavenging rather than physically protecting the surface of the cathode during cycling. These results may facilitate the design of the surface coating layer for high-voltage cathode materials and the application of electrolyte additives.

2. Results and Discussion

To better image the surface coating substances, the accelerating voltage in BSE mode was tuned, and the related results are shown in Figure S1 (Supporting Information). Backscattered mode detects the backscattered electrons, sensitive to atomic mass. The minimal voltage is 200 V (Figure S1f, Supporting Information), but it is not suitable for more accurate observation of the surface. The optimized voltage is 500 V (Figure S1e, Supporting Information) for the surface coating layer differentiation from the LNMO. Then, the surface coating process was optimized based on coverage and uniformity. The mixing time and sintering conditions were identified as influencing factors, and the results are listed in Figure S2 (Supporting Information). The coating process and calcination conditions are described in detail in the experiment session. Nanosized black dots are uniformly distributed around the single crystal at 450 °C but the black dot amount was reduced at 600 °C. When the temperature raises up to 700 °C, large black dots are generated on the surface. So, 600 °C is the optimized temperature for LBO coating on the LNMO surface. For checking the coating uniformity according to the dwell time, the minimum contrast is shown when the temperature is maintained for 10 h (Figure S2f, Supporting Information). After optimization,
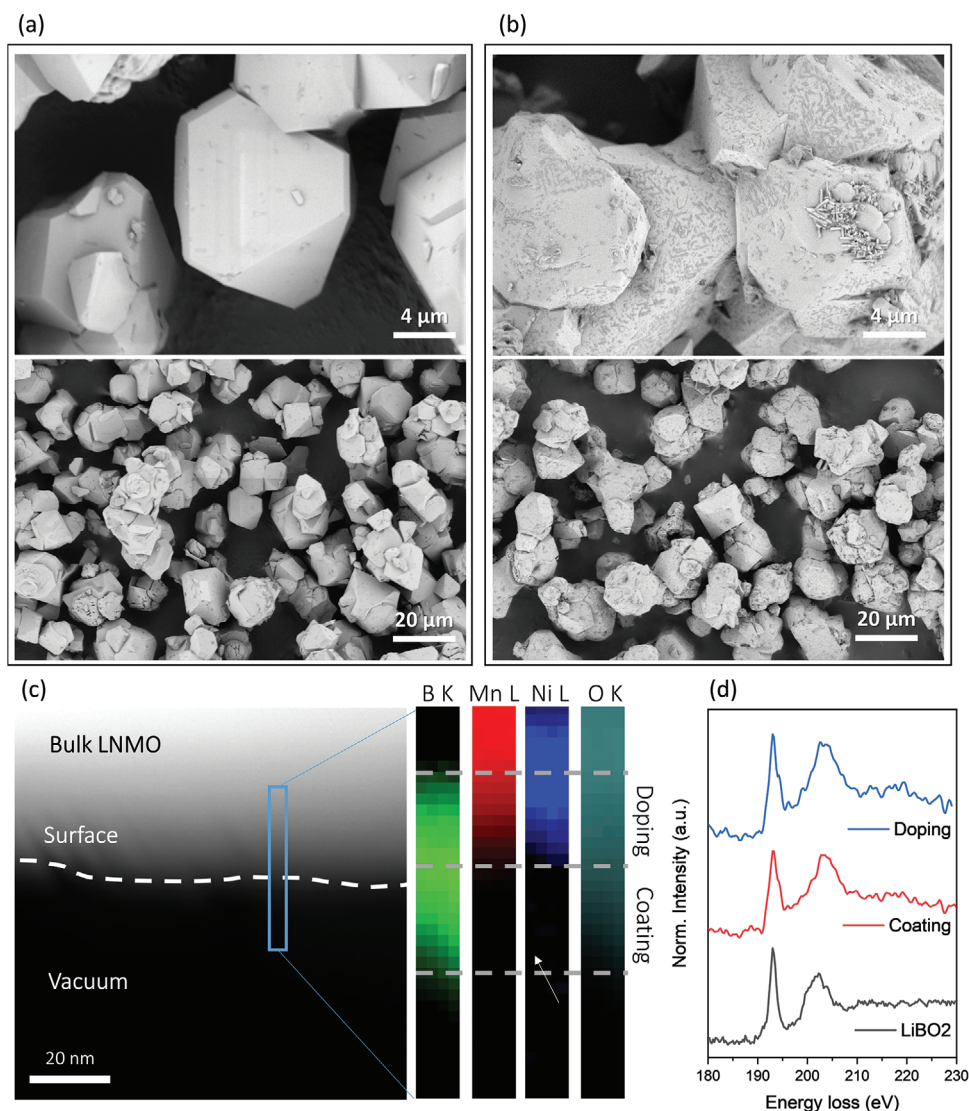
Figure 1. BSE images of a) uncoated and b) LBO-coated LNMO with the corresponding large views; c) STEM-EELS mapping results of LBO-coated LNMO sample; d) EELS spectra of boron corresponded to different locations.

the LBO-coated LNMO sample was synthesized with 10 g per batch for subsequent evaluation.

As shown in **Figure** 1a, the uncoated LNMO showed a uniform light grey color under BSE mode, and the particle size is ≈6–8 microns with typical single-crystal morphology. The uniform black dots can be observed from the LBO-coated LNMO powder in Figure 1b due to the surface coating substances with low atomic mass (borate species). We took low-magnification images with the same BSE mode and low accelerating voltage for large-scale coating uniformity evaluation. No dark agglomeration areas were observed, showing that low atomic mass species were well dispersed during the surface coating process.

We used STEM coupled with EELS mapping and spectra analysis to identify the chemical information of the boron coating, as shown in Figure 1c,d. The boron layer distribution was comprehensive. For the surface part, the boron layer without Ni/Mn on the LNMO surface was identified, suggesting that it was a

coating layer. At the same time, the boron overlap area with Ni and Mn was observed, suggesting that surface doping also occurred. The results indicate that boron coating can coexist with transition metal ions and act as a surface dopant. The Ni signal is attenuated by the atomic ratio, and the thickness of the sample would additionally diminish the Ni signal. Figure 1d indicates that the $LiBO_2$ surface dopant creates boron sites in a tetrahedral oxygen environment, as the energy loss peak position and shape are consistent with those of LBO coating materials. This suggests that $LiBO_2$ maintains its own phase without phase transition for coating and doping. Note that STEM-EELS was performed rather than EDS since boron is a light element that could hardly be excited with enough X-ray through the EDS detector. More results are shown in Figure S3 (Supporting Information). The consistent results showed that the boron element can be detected at a surface region like positions one and two but disappears at position three as the sub-surface. As for the Mn and Ni chemical environ-
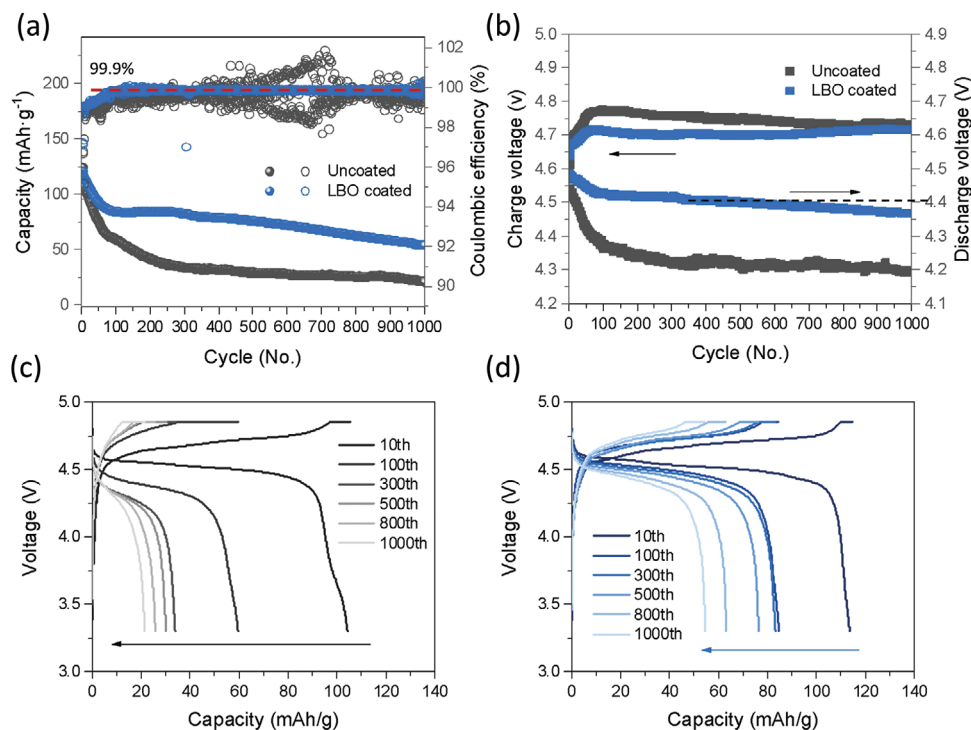
**ADVANCED
SCIENCE NEWS**

www.advancedsciencenews.com

**ADVANCED
FUNCTIONAL
MATERIALS**

www.afm-journal.de

Figure 2. a) full-cells cycling performances with b) the corresponding average charge/discharge voltage; the charge/discharge profiles of different cycles from c) uncoated and d) LBO-coated LNMO full cell.

ment, the EELS spectra indicated negligible changes. Therefore, the $LiBO_2$ surface coating layer on the LNMO was physically and chemically identified.

Full cells were assembled using uncoated LNMO and LBO-coated LNMO, and graphite was used as the anode. As shown in **Figure 2a**, the capacity retention after 1000 cycles is 18.1% for the uncoated LNMO and 46.1% for the LBO-coated LNMO. The uncoated LNMO shows a steep cycle slope up to ≈70 cycles in the beginning, followed by a large capacity drop in this interval and then an abrupt cycle degradation up to ≈300 cycles. In contrast, the LBO-coated LNMO shows slower degradation at the beginning, followed by a stable cycle slope after 100 cycles and a stable 99.9% Coulombic efficiency. It can be inferred that the side reaction with the electrolyte is minimized due to the borate coating layer. However, even LBO-coated LNMO experiences a drop in capacity retention within the initial 100 cycles. This phenomenon is primarily attributed to two main reasons. First, the full cells exhibit an initial phase stabilizing both the cathode and anode interphase. An early cycle retention drop is commonly observed in the full cell cycle performance. Secondly, this behavior is also attributed to the inherent characteristics of LNMO. LNMO is known to have poor long-term cycling performance, starting with a low initial Coulombic efficiency and a continuous degradation in efficiency. LBO-coated LNMO, while releasing LBO during cell operation, experiences ongoing degradation due to side reactions initiated by the electrochemical reaction of the carbonate baseline electrolyte at high voltage. Nevertheless, the dissolved LBO serves to alleviate the extent of degradation as cycling progresses. Figure 2b also shows that the LBO-coated LNMO has a more stable charge/discharge voltage from the be-

ginning, demonstrating its improved performance. The results of cycling at room temperature, as well as at elevated temperatures (45 °C), demonstrate that LBO-coated LNMO exhibits a consistently stable initial slope even at higher temperatures (Figure S4a, Supporting Information). This is further corroborated by the remarkably stable average discharge voltage plot (Figure S4b, Supporting Information). Figure 2c,d shows the charge–discharge profiles of uncoated and LBO-coated LNMO full cells. The charge plateau of uncoated LNMO cells shifts to a higher voltage region while the discharge plateau shifts to a lower region, suggesting an increase in internal impedance, while both the charge and discharge capacity drop quickly, which implies fast active lithium inventory loss. The charge and discharge plateau of LBO-coated LNMO shifts much less than the uncoated sample, meaning the LBO coating plays a significant role in controlling the internal impedance. As for the length of the constant voltage (CV) section at 4.85 V, LBO-coated LNMO remained the same with the cycling, while the uncoated LNMO CV section stretched from 100 cycles. The escalation observed in the CV section signifies an elevation in internal impedance. In the context of $V = IR$, a prolonged CV segment under consistent current cut-off conditions suggests a proportional rise in resistance.[24] This suggests that lithium from the cathode was not sufficiently de-intercalated during charging, resulting in low and unstable Coulombic efficiency.

To understand the mechanism of LiF the LBO surface coating can dramatically improve the cycling stability of LNMO/Gr full cells, different characterizations were performed to track boron inside the cells. First, soaking tests were performed with uncycled electrodes for boron dissolution. The uncoated LNMO and LBO-coated LNMO electrodes were soaked in the fresh electrolyte
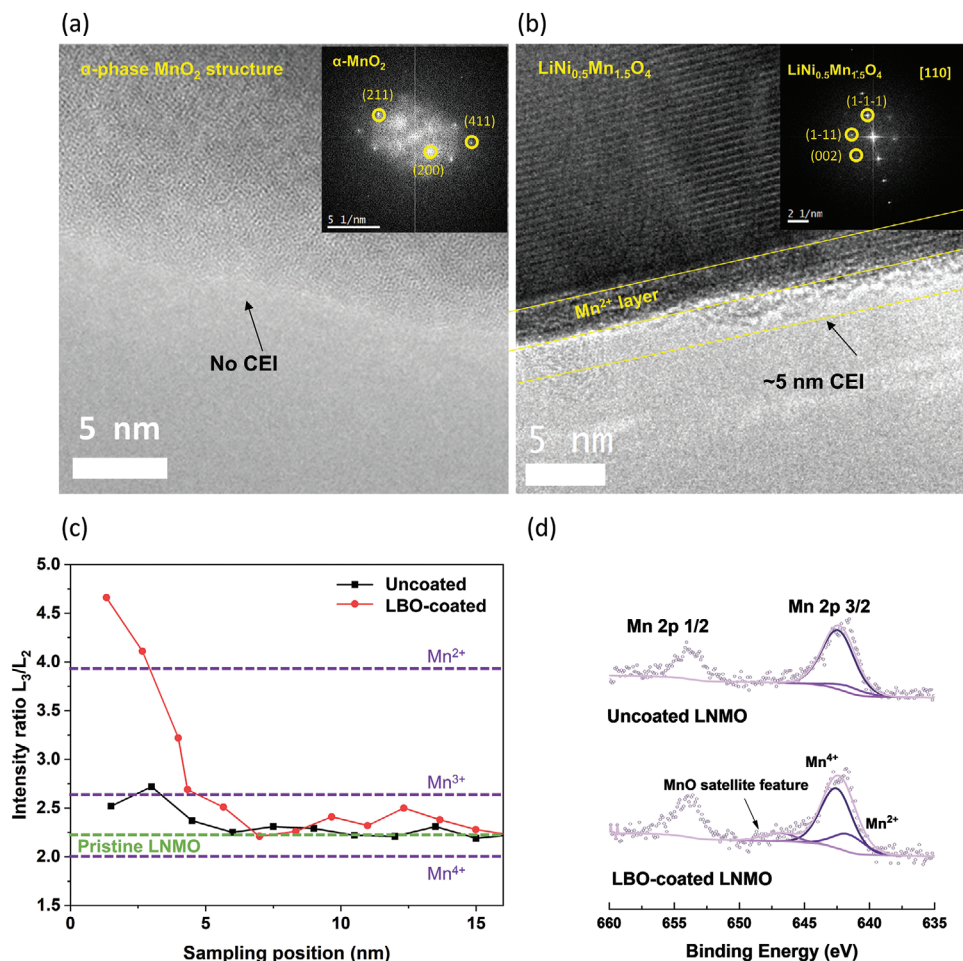
**ADVANCED
SCIENCE NEWS**

www.advancedsciencenews.com

**ADVANCED
FUNCTIONAL
MATERIALS**

www.afm-journal.de

Figure 3. TEM with SAED results of a) uncoated and b) LBO-coated LNMO after 1000 cycles. c) EELS Mn Spectra and d) XPS spectra of Mn 2p of uncoated and LBO-coated LNMO after 1000 cycles.

for 24 h, and the supernatant was fetched and diluted for the ICP-MS test. The detailed experiment setup can be found in Figure S4 (Supporting Information). As shown in Figure S5 (Supporting Information), the $LiBO_2$ coating layer can be partially dissolved by the baseline electrolyte before cycling, resulting in the loss of about 60 wt.% of the total coating mass. The cycled electrodes were also investigated. The soluble boron species are uniformly distributed in the cathode and anode after long-term cycling, as shown in Figure S5a (Supporting Information). Meanwhile, no floating Ni/Mn from cycled graphite with LBO-coated LNMO was detected (Figure S5b, Supporting Information). This implies that the boron species mitigated the cross-talk issues between the LNMO cathode and graphite anode. Second, XPS was performed to understand the chemical status of the interphase, and the results are shown in Figure S6 (Supporting Information). After long-term cycling, cathode interphase components were almost the same for both the uncoated and LBO-coated LNMO, except for the minor difference from the P 2p signal. Both samples showed a lattice oxygen peak around 684.5 eV in O 1s spectra, implying a thin CEI. The uncoated sample showed an obvious P—F signal, while the LBO-coated sample did not, which may be related to salt residual on the sample surface. Figure S6b (Sup-

porting Information) shows the SEI information on the anode, and several distinctive features have been detected. The first one is the Li-O peak in O 1s spectra, which remained in the graphite paired with the LBO-coated LNMO while not appearing in the uncoated case. This implies that the electrode corrosion is stronger in the uncoated LNMO cell than in the LBO-coated LNMO cell. The second is the metal-F peak around 684.5 eV in F 1s spectra. The graphite paired with uncoated LNMO showed a stronger peak, which refers to a higher metal fluoride content than the graphite paired with LBO-coated LNMO. The third is the Mn 2p spectra; the graphite with uncoated LNMO has an obvious Mn signal, while the graphite paired with LBO-coated LNMO does not, suggesting the cross-talk between cathode and anode in the uncoated cell was stronger than the LBO coated cell. The XPS results are consistent with ICP-MS results.

TEM was performed on the cathode surface to compare the uncoated and LBO-coated LNMO. As shown in **Figure 3**, both samples showed degradation on the surface after 1000 cycles. While the uncoated LNMO shows no CEI with severe phase change (Figure 3a), the LBO-coated LNMO had limited phase change with CEI, and no boron was detected (Figure 3b). In the case of the uncoated LNMO, the cathode surface was found to be in
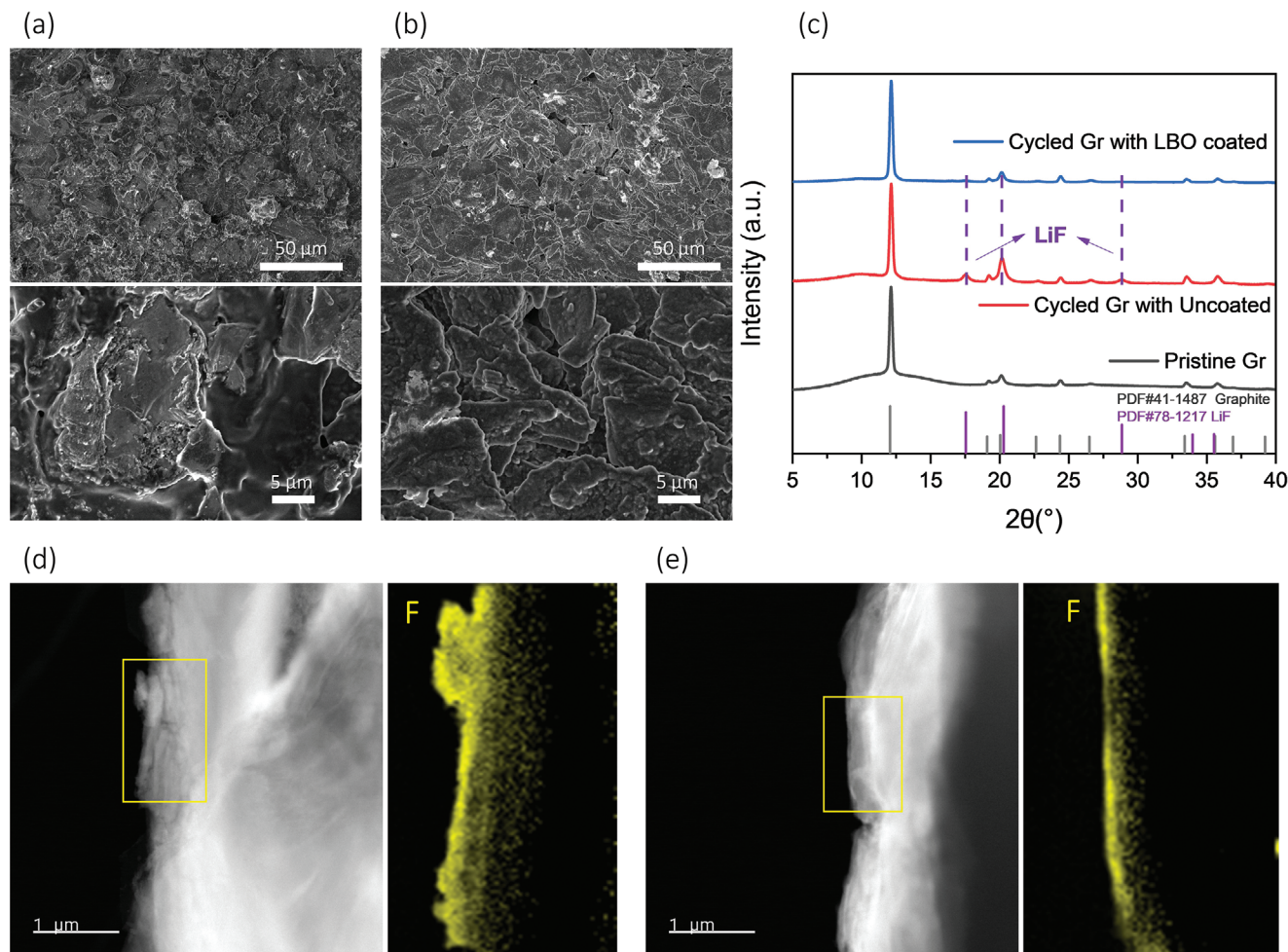
**ADVANCED
SCIENCE NEWS**

www.advancedsciencenews.com

**ADVANCED
FUNCTIONAL
MATERIALS**

www.afm-journal.de

Figure 4. SEM images of graphite surface paired with a) uncoated and b) LBO-coated LNMO; c) XRD results of different graphite powders. EELS fluorine (F) mapping graphite paired with d) uncoated LNMO (after 1000 cycles) and e) LBO-coated LNMO (after 1000 cycles).

the disordered MnO_2, as confirmed by both lattice fringe and selected area electron diffraction (SAED), as the [200], [211], and [411] diffraction patterns corresponding to the α-phase MnO_2 structure[25,26] and the disordered phase were identified. The absence of CEI may indicate severe corrosion from the degraded electrolyte. However, in the case of the LBO-coated LNMO, the bulk structure slightly changed into a more disordered phase but maintained the spinel feature at a thickness of 5 nm, as the [110] diffraction pattern was still observed. This suggests that surface coating with boron can improve long-term cycling by controlling the outermost phase transition and helping to mitigate corrosion from the electrolyte. To further verify the Mn valence on the surface, EELS were performed and the related data are shown in Figure S7 (Supporting Information), the intensity ratio of L3 and L2 peaks were calculated as shown in Figure 3c. After 1000 cycles, Mn^{2+} still exists up to about 3 nm from the surface of LBO-coated LNMO, but no more Mn^{2+} exists in uncoated LNMO. This implies that the transition metal including Mn was dissolved into the electrolyte and induced obvious cross-talk phenomena, further redeposited on the surface of the anode. XPS shown in Figure 3d confirmed the different Mn valences from uncoated and LBO-coated LNMO surfaces. For the LBO-coated

LNMO sample, a MnO satellite feature ($\approx$647 eV) as well as the high Mn^{2+} ratio proved the Mn^{2+} existence[27] as consistent with the STEM and EELS spectra results. Further investigations on the chemical information of boron from the LBO-coated LNMO after 1000 cycles were performed via EELS spectra, as shown in Figure S8 (Supporting Information). It could be confirmed that there was no boron signal on the particle, which means that the borate surface coating was completely dissolved/detached from the LNMO surface. The results align well with the previous results, where half of the boron elements would be dissolved into the electrolyte only by soaking overnight. This indicates that the physical separation between LNMO and degraded electrolyte by borate coating needs additional explanations.

The presence or absence of coating on the cathode side significantly impacts the chemical reactions occurring in the full cell through the anode. To investigate the cross-talk effect between the cathode and anode, we performed post-mortem SEM and XRD analysis, as shown in **Figure 4**. The graphite paired with the uncoated LNMO has a larger number of by-products on its surface, covering the graphite particles (Figure 4a), while the graphite paired with the LBO-coated LNMO has little by-product (Figure 4b). We further conducted XRD on the collected graphite
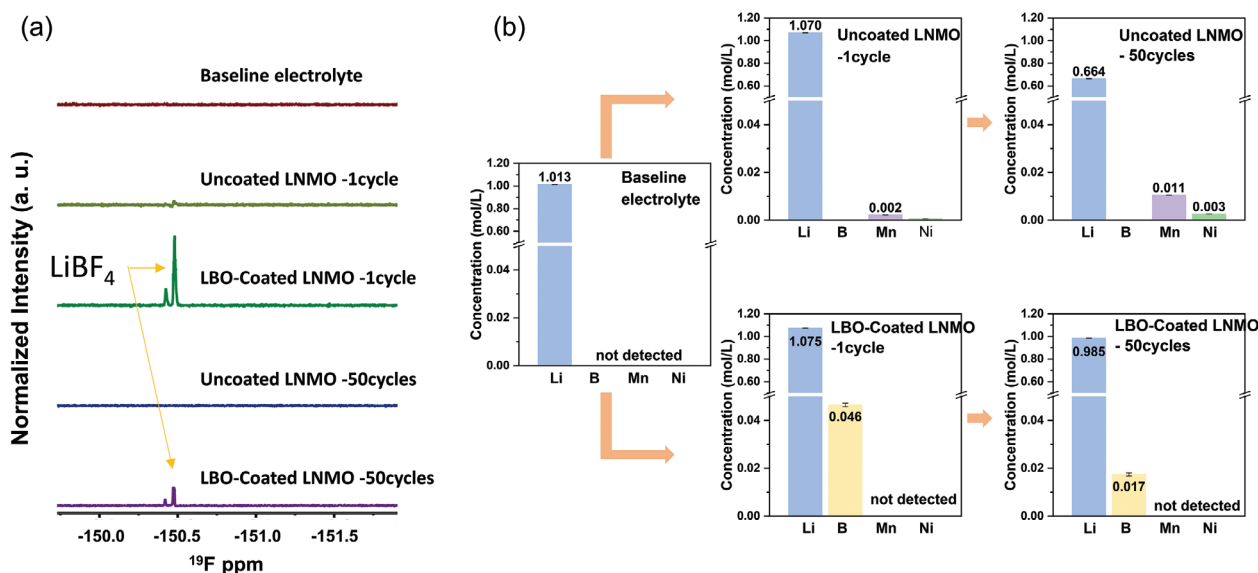
ADVANCED
SCIENCE NEWS

www.advancedsciencenews.com

ADVANCED
FUNCTIONAL
MATERIALS

www.afm-journal.de

Figure 5. a) ^{19}F-NMR and b) ICP-MS from different electrolyte samples, including pristine baseline and cycled electrolytes from uncoated/LBO-coated LNMO after 1 cycle and 50 cycles.

powder to identify the chemical composition of the by-products. The XRD results identified the presence of crystal LiF with the graphite, as peaks corresponding to LiF are observed (Figure 4c). Such a large amount of LiF may result from severe anode SEI corrosion, which consumes active Li and degrades the cycling performance.[28,29] LiF itself does not induce corrosion in the electrode; rather, the adverse consequences stem from chemical reactions leading to LiF formation, warranting concern. To expound, the high-voltage decomposition reaction between $LiPF_6$ and carbonate-based electrolytes swiftly produces HF and H_2O, culminating in LiF formation. Thus, the substantial presence of LiF within the SEI layer substantiates the heightened activity of the electrolyte decomposition reaction in the full-cell system, signifying a more robust progression of electrode corrosion. EELS fluorine elemental mapping was performed. Graphite paired with uncoated LNMO showed much thicker fluorine layers on the surface than the graphite paired with LBO-coated LNMO, with obvious particle shape (Figure 4d,e). Additional images can be found in the supplementary information (Figure S9, Supporting Information). This result is consistent with SEM and XRD results that boron surface coating can alleviate the continuous growth of SEI.

Such obvious differences induced by different cathodes bring up the necessity for electrolyte investigations because the electrolyte is the only medium for the cross-talk phenomenon. Therefore, single-layer pouch cells were assembled using the uncoated and LBO-coated LNMO, and the specifications are listed in Table S2 (Supporting Information). The electrochemical performances of pouch cells are shown in Figure S10a (Supporting Information). LBO-coated LNMO pouch cells showed better cycling performance than uncoated LNMO pouch cells, which is consistent with coin cells. The pouch cells were disassembled in the glovebox after 50 cycles and then placed into the sealed centrifuge tube for electrolyte collection. Another set of identical pouch cells cycled 1 time was prepared as the reference

sample, and the electrolytes from these two cells were also collected. The collected electrolytes from different cells are shown in Figure S10b (Supporting Information). The uncoated LNMO consumed more electrolytes than the LBO-coated LNMO, and the color was also much darker, indicating severe decomposition. The collected electrolytes were diluted for ICP-MS and ^{19}F-NMR analysis.

To understand the mechanism behind the improved cycling performance of the LBO-coated LNMO, we focused on the dissolution of transition metals and the behavior of boron-related species. Pouch cells were assembled and the electrolyte solutions were collected from the opened cells after different numbers of cycles. The cell's electrolyte was collected after the first formation cycle to identify the degradation mechanism at the beginning of the cycle, and the cells were disassembled after 50 cycles to observe the changes in species over time. The results of ^{19}F-NMR and ICP-MS analysis are shown in **Figure 5**.

In the ^{19}F-NMR analysis (Figure S11, Supporting Information), the LBO-coated LNMO is found to contain $LiBF_4$ peaks ≈-150 ppm after just one cycle at C/3, indicating that the $LiBO_2$ coating layer can be partially dissolved and converted into BF_4^- during cycling. The concentration of boron in the form of BF_4^- decreased after cycling (Figure 5a) and was uniformly deposited on both the cathode and anode. This suggests that B—F bonding had already been formed even after just one charge/discharge cycle. It is also confirmed that this forms the CEI/SEI layer and is involved in the cycle degradation mechanism by being dissolved in the electrolyte. If B—F bonding is not formed, the decomposed fluorine will form HF or LiF and accelerate cycle degradation.

In the ICP-MS analysis, the uncoated LNMO cell showed significant dissolution of Ni and Mn even after the first cycle at C/3, with concentrations of 12 ppb Ni and 48 ppb Mn after 50 cycles. The lithium concentration in the electrolyte also decreased significantly from the original ≈580 to 378 ppb. This indicates a loss of lithium inventory in the electrolyte. In contrast, the LBO-coated
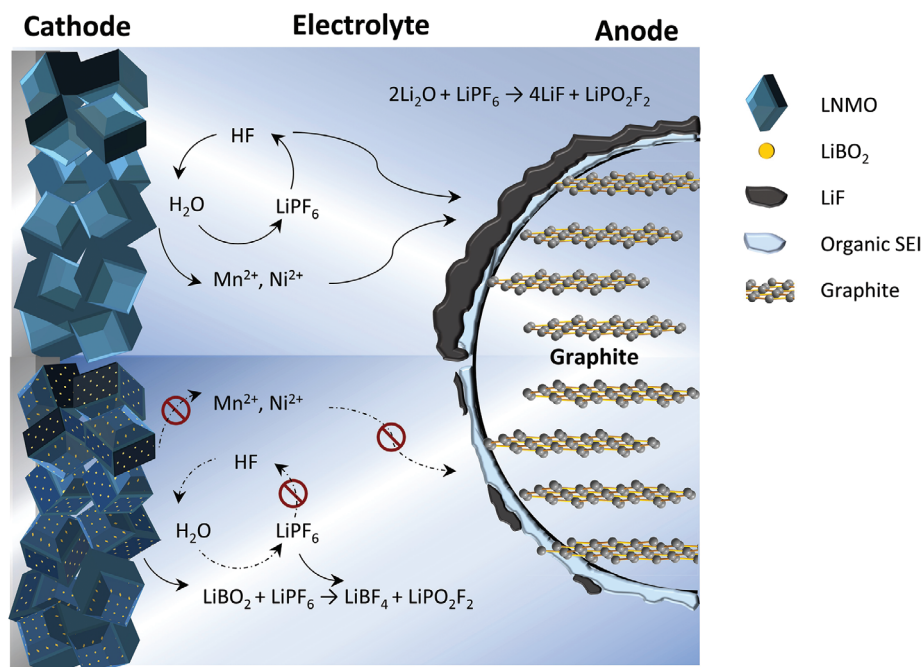
ADVANCED
SCIENCE NEWS

www.advancedsciencenews.com

ADVANCED
FUNCTIONAL
MATERIALS

www.afm-journal.de

Figure 6. Schematics of performance improvement by LBO-coated LNMO in LNMO/Gr full cell.

LNMO showed Ni and Mn concentrations below the detection limit, and the lithium concentration in the electrolyte remained relatively stable after 50 cycles. The boron concentration was also monitored via ICP-MS analysis, and no transition metals were dissolved in the electrolyte of the LBO-coated LNMO pouch cell as the lithium concentration. The amount of lithium after the first formation is almost the same. However, after 50 cycles, it was confirmed that the concentration decreased as more lithium was used for cycle degradation. The boron increased to 41 ppb after 1 cycle at C/3 and dropped to 15 ppb after 50 cycles, showing that the concentration became lower along with more cycles. The boron species in the electrolyte would be consumed along with the cycling.

The detailed mechanism of boron species helps improve the high voltage cell as shown in **Figure 6**. $LiPF_6$ and the solvent are constantly decomposed during high-voltage cycling, generating by-products such as water and HF.[6] The acid will corrode the cathode material as transition metal ions are dissolved and deposited on the anode simultaneously. The degraded electrolyte will also lead to the overgrowth of SEI layers that consume active lithium. However, in the case of the LBO-coated LNMO, borate radicals from the coating layer decomposition can effectively prevent salt decomposition by forming $LiBF_4$ species. The bonding related to boron and fluorine appeared only in the LBO-coated LNMO. The formation energy of BF_4^- (-1710 kJ mol^{-1}) is much lower than that of HF (-273 kJ mol^{-1}), making this reaction thermodynamically favorable. In addition, the B—F bond (613 kJ mol) has a higher bond energy than the H—F (565 kJ mol^{-1}) and P—F (490 kJ mol^{-1}) bonds, meaning that the B—F bond is more stable.[30] As a result, less HF corrosion occurs in the LBO-coated LNMO cell, leading to uniform CEI/SEI. The well-preserved CEI/SEI layers then lead to reduced transition metal dissolution and deposition in the cell, all of which contribute to improved

cell cycling stability. In summary, Figure 5 demonstrates that the $LiBO_2$ surface coating mainly functions as an LBO reservoir to mitigate salt decomposition in the electrolyte during cycling, mitigating the cross-talk between the cathode and anode. The cycle degradation mechanism in LIBs was found to preferentially occur through a chemically stable reaction under the presence of boron species. Understanding the mechanism of boron can provide insight into future improvements for high-voltage cell cycle stability.

3. Conclusion

$LiBO_2$ was successfully coated on the surface of single-crystal LNMO cathode materials. The surface coating uniformity was evaluated via BSE-SEM methods, and the related chemical environment of boron species was characterized via STEM-EELS. It was identified that the surface boron species were in nano-sized particles and well distributed on the LNMO surface. Furthermore, the boron elements existed both as surface doping and coating. The electrochemical performances of LBO-coated LNMO were compared with the uncoated sample in full cells for 1000 cycles, and the coated sample outperformed the uncoated one. The surface boron species fully dissolved into electrolytes after long-term cycling. ^{19}F-NMR and ICP-MS results from electrolyte showed that $LiBO_2$ started to dissolve and turned into $LiBF_4$. This process can dramatically prevent salt decomposition. Consequently, the cross-talk phenomena between the cathode and anode were mitigated, and both CEI/SEI were well preserved. We believe these findings can be applied to other high-voltage cathode materials and contribute to the commercialization of next-generation high-voltage LIBs. This work may also inspire future research to stabilize the $LiPF_6$-carbonate-based elec-

trolytes through cathode surface coating and electrolyte additive design.

4. Experimental Section

Sample Preparation: A pristine LNMO sample was provided by Umicore. For coating material synthesis, 0.03 M of Polyvinylpyrrolidone (PVP) was added (MW = 50 000) to 100 mL of tetraethylene glycol (TTEG). The remaining PVP in the solution was properly dissolved. LiOH H_2O (0.015 M) was added and waited until it dissolved and 0.015 M of H_3BO_3 was added and then the heat was raised to 80 °C. After 2 h of reaction, let it naturally cool, then wash it in ethanol seven times. After removing moisture in an 80 °C vacuum oven for a day, ground it finely using a mortar and pestle, and finally, a ball mill was used to make it small at 500 rpm for 5 h with ethanol. Dried again in a vacuum oven at 80 °C for a day and ground with a mortar and pestle. Measure $LiBO_2$ suitable for 2wt.% in a weight ratio of cathode and physically mix the cathode with a Thinky Mixer (Thinky Corporation) at 2000 rpm for 10 min. Put the well-mixed powder into the furnace, set the temperature raising condition to 600 °C at 5 °C h^{-1}, and maintain it at 600 °C for 10 h, and the same temperature condition as raising the temperature to lower the temperature to room temperature (20 °C). After calcination, the powder was evenly ground using a mortar and pestle for ≈10 min. FEI Apreo was applied with 5 kV as the accelerating voltage and 0.1 nA as the beam current for the SEM analysis. A backscattered electron imaging technique was applied to verify the uniformity of the $LiBO_2$ surface coating layer on single-crystal LNMO, especially for large-area coating uniformity evaluation. The microscope detector was first changed to backscattered mode, which was extremely sensitive to backscattered electrons. Then, the accelerated voltage was lowered to detect the surface information well. The contrast gradually appeared when lowering the accelerated voltage from 5 kV to 200 V, while the optimized voltage was 500 to 1000 V to acquire clear images.

Electrode Preparation: To evaluate the electrochemical performance of LBO-coated LNMO, electrodes using uncoated and LBO-coated LNMO were prepared, with SPC65 (carbon black, TIMCAL Ltd.) as the conductive agent and HSV900 (PVDF, Arkema Inc.) as the binder, in a mass ratio of 90:5:5 and a cathode loading of 3 mAh cm^{-2}. The mix was then well dissolved in a proper amount of N-methyl-2-pyrrolidone (NMP, ≥99%, Sigma–Aldrich) and mixed with a Thinky Mixer to form the slurry. The slurry was cast onto Al foil and dried at 80 °C in a vacuum oven overnight, followed by 1 h of 120 °C drying at elevated temperature. The electrode was punched into cathode discs with a 12.7 mm diameter and a loading of active mass ≈24 mg cm^{-2}. For LNMO/Gr full cells, both CR2032 and pouch cells were assembled. Ningbo Institute of Materials Technology & Engineering (NIMTE) provided the graphite electrode used in this work with an active mass ratio of 94%. For CR2032 full cells, the graphite electrode was punched into anode discs with a 13 mm diameter, and the designed N/P ratio was ≈1.1. For pouch-type full cells, the cathode size was 44 × 30 mm, and the anode size was 45 × 32 mm. For all the cells, Celgard 2325 was used as the separator. 1 M $LiPF_6$ in EC: EMC = 3:7 (vol%) was obtained from Gotion, USA, and was denoted as baseline electrolyte in the following sessions. All the coin cells were assembled in the Ar-filled glovebox with moisture control (H_2O < 0.5 ppm), and 50 μL of electrolyte was used for each coin cell. The pouch cells were first assembled in the atmosphere without electrolytes. Afterward, the pouch cell was moved to a heating tray inside the glovebox antechamber and dried at 80 °C overnight under vacuum before the electrolyte injection. After drying, the dry pouches were moved inside the Ar-filled glovebox without air exposure, and 500 μL of electrolyte was injected into each cell. The pouch cells with electrolytes were vacuum-sealed inside the glovebox and moved out for further testing.

Electrochemical Performance Evaluation: After assembling, the coin cell(CR2032) and pouch cell full cells were evaluated by cycling them at a rate of C/3 (where 1C is 147 mA g^{-1}) after two formation cycles at C/10. The electrochemical performances of all the cells were tested at room tem-

perature either by the Neware Battery Test System (Neware Technology Ltd., China) or Arbin BT2000 instruments (Arbin instrument, USA).

Characterizations: The cycled cells were disassembled in the glovebox to prevent air exposure. After long-term cycling, the cycled glass fiber became sticky to graphite, so a surgical blade was used to separate most of them and scratch the residual fiber from the graphite side. XPS analysis was performed using a Kratos AXIS Supra. All the cycled electrodes were prepared without washing, and the transfer process was air-tight to avoid any possible degradation. The XPS was operated using an Al anode source at 15 kV with a 10^{-8} Torr vacuum level. All XPS measurements were collected using an auto-neutralizer during acquisition. Survey scans were collected with a 1.0 eV step size, followed by high-resolution scans with a step size of 0.1 eV. All the data were calibrated using a C 1s peak at 284.6 eV. ICP-MS analysis was performed with a Thermo iCAP RQ ICP-MS to analyze the elemental concentration in fresh and cycled electrolytes. ^{19}F-NMRs were conducted on electrolytes to analyze the salt species in the electrolyte. The ^{19}F-NMR measurements of the electrolyte samples were performed with a Jeol ECA 500 spectrometer. Liquid NMR samples were prepared by adding 10 μL of electrolyte to 600 μL of DMSO-D6 solution, and 50 μL of α, α, α-trifluorotoluene was added to each sample as the reference and sealed in an NMR tube inside the Ar-filled glovebox for further measurement. The NMR spectrums were analyzed with MestReNova. All spectrums were calibrated with α, α, α-trifluorotoluene at −63.72 ppm. TEM analysis was performed on a field emission gun JEOL2800 at 200 kV with Gatan OneView Camera (full 4k × 4k resolution). STEM and EELS were performed on primary particles at the annular dark-field (ADF) mode using a JEOL JEM-ARM300CF at 300 kV, equipped with double correctors. To minimize possible electron beam irradiation effects, EELS spectra presented in this work were acquired from areas without pre-beam irradiation.

Supporting Information

Supporting Information is available from the Wiley Online Library or from the author.

Conflict of Interest

The authors declare no conflict of interest.

Data Availability Statement

The data that support the findings of this study are available from the corresponding author upon reasonable request.

[1] R. Schmuch, R. Wagner, G. Hörpel, T. Placke, M. Winter, *Nat. Energy* **2018**, *3*, 267.

[2] T. Ohzuku, S. Takeda, M. Iwanaga, *J. Power Sources* **1999**, *81*, 90.

[3] G. Liang, Z. Wu, C. Didier, W. Zhang, J. Cuan, B. Li, K.-Y. Ko, P.-Y. Hung, C.-Z. Lu, Y. Chen, G. Leniec, S. M. Kaczmarek, B. Johannessen, L. Thomsen, V. K. Peterson, W. K. Pang, Z. Guo, *Angew. Chem., Int. Ed.* **2020**, *59*, 10594.

[4] D. Aurbach, B. Markovsky, Y. Talyossef, G. Salitra, H.-J. Kim, S. Choi, *J. Power Sources* **2006**, *162*, 780.

[5] W. Li, Y.-G. Cho, W. Yao, Y. Li, A. Cronk, R. Shimizu, M. A. Schroeder, Y. Fu, F. Zou, V. Battaglia, A. Manthiram, M. Zhang, Y. S. Meng, *J. Power Sources* **2020**, *473*, 228579.

[6] K. Xu, *Chem. Rev.* **2014**, *114*, 11503.

[7] H. Lee, S. Choi, S. Choi, H.-J. Kim, Y. Choi, S. Yoon, J.-J. Cho, *Electrochem. Commun.* **2007**, *9*, 801.

[8] W. Liu, J. Li, W. Li, H. Xu, C. Zhang, X. Qiu, *Nat. Commun.* **2020**, *11*, 3629.

[9] A. Cimini, O. Palumbo, E. Simonetti, M. De Francesco, G. B. Appetecchi, S. Fantini, R. Lin, A. Falgayrat, A. Paolone, *J. Therm. Anal. Calorim.* **2020**, *142*, 1791.

[10] J. Im, J. Lee, M.-H. Ryou, Y. M. Lee, K. Y. Cho, *J. Electrochem. Soc.* **2017**, *164*, A6381.

[11] T. Noguchi, T. Hasegawa, H. Yamauchi, I. Yamazaki, K. Utsugi, *ECS Trans.* **2017**, *80*, 291.

[12] N. Ehteshami, E. Paillard, *ECS Trans.* **2017**, *77*, 11.

[13] F. Ulu Okudur, J. D'Haen, T. Vranken, D. de Sloovere, M. Verheijen, O. M. Karakulina, A. M. Abakumov, J. Hadermann, M. K. van Bael, A. Hardy, **2018**, *RSC Adv.*, *8*, 7287.

[14] H. Duncan, B. Hai, M. Leskes, C. P. Grey, G. Chen, *Chem. Mater.* **2014**, *26*, 5374.

[15] Z. J. Liang, R. Liang, Z. B. Wang, Y. Xue, F. d. Yu, D. Liu, Y. X. Zhou, *Ionics* **2017**, *23*, 35.

[16] E. R. Østli, Y. Tesfamhret, S. Wenner, M. J. Lacey, D. Brandell, A. M. Svensson, S. M. Selbach, N. P. Wagner, *ACS Omega* **2021**, *6*, 30644.

[17] J. Y. Piao, L. Gu, Z. Wei, J. Ma, J. Wu, W. Yang, Y. Gong, Y. G. Sun, S. Y. Duan, X. Tao, D. S. Bin, A. M. Cao, L. J. Wan, *J. Am. Chem. Soc.* **2019**, *141*, 4900.

[18] T. Noguchi, I. Yamazaki, T. Numata, M. Shirakata, *J. Power Sources* **2007**, *174*, 359.

[19] J. Chong, S. Xun, X. Song, G. Liu, V. S. Battaglia, *Nano Energy* **2013**, *2*, 283.

[20] J. Y. Shi, C. W. Yi, K. Kim, *J. Power Sources* **2010**, *195*, 6860.

[21] R. Zhu, S. Zhang, Q. Guo, Y. Zhou, J. Li, P. Wang, Z. Gong, *Electrochim. Acta* **2020**, *342*, 136074.

[22] J. S. Chae, S. B. Yoon, W. S. Yoon, Y. M. Kang, S. M. Park, J. W. Lee, K. C. Roh, *J. Alloys Compd.* **2014**, *601*, 217.

[23] H. W. Chan, J. G. Duh, S. R. Sheen, *Surface and Coatings Technology* **2004**, *188*, 116.

[24] K. Liu, C. Zou, K. Li, T. Wik, *IEEE Trans Industr Inform* **2018**, *14*, 5463.

[25] R. A. Davoglio, G. Cabello, J. F. Marco, S. R. Biaggio, *Electrochim. Acta* **2018**, *261*, 428.

[26] H. Y. Lin, Y. P. Sun, B. J. Weng, C. T. Yang, N. T. Suen, K. H. Liao, Y. C. Huang, J. Y. Ho, N. S. Chong, H. Y. Tang, *Electrochim. Acta* **2007**, *52*, 6548.

[27] M. C. Biesinger, B. P. Payne, A. P. Grosvenor, L. W. M. Lau, A. R. Gerson, R. S. C. Smart, *Appl. Surf. Sci.* **2011**, *257*, 2717.

[28] N. S. Choi, J. G. Han, S. Y. Ha, I. Park, C. K. Back, *RSC Advances* **2015**, *5*, 2732.

[29] H. Wang, X. Xie, X. Wei, X. Zhang, J. Zhang, Y. Huang, Q. Li, *ACS Appl. Mater. Interfaces* **2017**, *9*, 33274.

[30] Y. Li, W. Li, R. Shimizu, D. Cheng, H. N. Nguyen, J. Paulsen, S. Kumakura, M. Zhang, Y. S. Meng, *Adv. Energy Mater.* **2022**, *12*, 2103033.